

pubs.acs.org/JACS Article

C-N Bond Forming Radical Rebound Is the Enantioselectivity-Determining Step in P411-Catalyzed Enantioselective C(sp³)-H Amination: A Combined Computational and Experimental Investigation

Binh Khanh Mai, Natalia M. Neris, Yang Yang,* and Peng Liu*



Cite This: J. Am. Chem. Soc. 2022, 144, 11215–11225



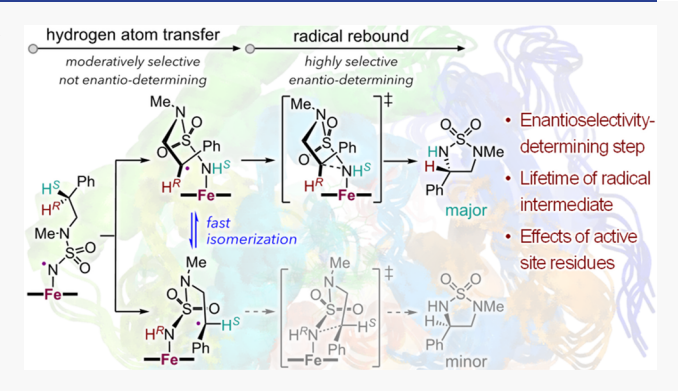
ACCESS I

Metrics & More

Article Recommendations

Supporting Information

ABSTRACT: Engineered metalloenzymes represent promising catalysts for stereoselective C–H functionalization reactions. Recently, P450 enzymes have been evolved to allow for new-to-nature intramolecular C(sp³)–H amination reactions via a nitrene transfer mechanism, giving rise to diamine derivatives with excellent enantiocontrol. To shed light on the origin of enantioselectivity, a combined computational and experimental study was carried out. Hybrid quantum mechanics/molecular mechanics calculations were performed to investigate the activation energies and enantioselectivities of both the hydrogen atom transfer (HAT) and the subsequent C–N bond forming radical rebound steps. Contrary to previously hypothesized enantioinduction mechanisms, our calculations show that the radical rebound step is enantioselectivity-



determining, whereas the preceding HAT step is only moderately stereoselective. Furthermore, the selectivity in the initial HAT is ablated by rapid conformational change of the radical intermediate prior to C-N bond formation. This finding is corroborated by our experimental study using a set of enantiomerically pure, monodeuterated substrates. Furthermore, classical and ab initio molecular dynamics simulations were carried out to investigate the conformational flexibility of the carbon-centered radical intermediate. This key radical species undergoes a facile conformational change in the enzyme active site from the pro-(R) to the pro-(S) configuration, whereas the radical rebound is slower due to the spin-state change and ring strain of the cyclization process, thereby allowing stereoablative C-N bond formation. Together, these studies revealed an underappreciated enantioinduction mechanism in biocatalytic $C(sp^3)-H$ functionalizations involving radical intermediates, opening up new avenues for the development of other challenging asymmetric $C(sp^3)-H$ functionalizations.

INTRODUCTION

Due to the ubiquity of C-H bonds in organic molecules, selective C-H functionalization reactions hold the potential to significantly streamline organic synthesis. Over the past decade, extensive efforts have been devoted to the development of catalytic asymmetric functionalization of C(sp³)-H bonds.2 Among these C-H functionalization processes, asymmetric C-H amination is particularly attractive, as it allows for the rapid assembly of chiral amines that are found in a range of important pharmaceuticals and agrochemicals. Owing to their exquisite control over reaction stereochemistry, biocatalytic methods have recently emerged as an appealing alternative to stereoselective $C(sp^3)$ -H functionalization. Over the past 8 years, the groundbreaking work from Arnold, Fasan, Hartwig, and many other researchers has culminated in a range of enantioselective C(sp³)-H amination processes using a metalloenzyme-catalyzed nitrene transfer mechanism.⁵ In these $C(sp^3)$ -H amination reactions, using nitrene

precursors including organic azides and hydroxylamine esters, a putative metal nitrene intermediate forms in the enzyme's active site, enabling further $C(sp^3)-H$ amination in a stereoselective fashion. ^{6,7}

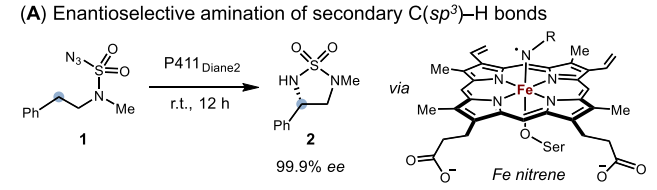
In recent years, the Arnold group engineered "P411" enzymes, a class of cytochromes P450 featuring an iron-binding serine residue, to facilitate asymmetric $C(sp^3)$ –H amination processes. ^{6a–g} In 2019, a set of P411 nitrene transferases were developed for the asymmetric intramolecular amination of primary, secondary, and tertiary $C(sp^3)$ –H bonds. ^{6e} With P411_{Diane2}, cyclic 1,2-diamine derivatives formed

Received: February 28, 2022 Published: May 18, 2022

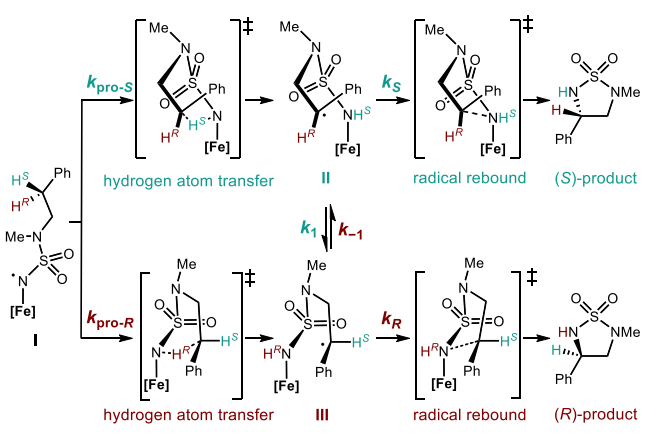




with excellent enantioselectivity via the asymmetric functionalization of secondary C(sp³)-H bonds (Figure 1A). Our



(B) Mechanisms of enantioinduction



Possible Scenarios

	HAT (C–H cleavage)	radical rebound	
(i) $k_1, k_{-1} << k_S, k_R$	 enantioselectivity- determining 	 retention of stereochemistry 	
(ii) $k_1, k_{-1} >> k_S, k_R$	 ablation of stereochemistry after HAT 	 enantioselectivity- determining 	

<u>Goals</u>

- · Mechanism and enantioselectivity-determining step
- · Lifetime and conformational flexibility of radical intermediate
- · Effects of active site residues on reactivity and enantioselectivity

Figure 1. Possible mechanisms of enantioinduction in the engineered $P411_{Diane2}$ -catalyzed asymmetric amination of secondary $C(sp^3)$ -H bonds.

previous density functional theory (DFT) calculations using an Fe-porphine model complex indicated a stepwise mechanism involving an Fe nitrene-mediated hydrogen atom transfer (HAT) and a subsequent radical rebound step, leading to $C(sp^3)-N$ bond formation products. To date, the enantioselectivity-determining step in this intramolecular secondary $C(sp^3)-H$ amination process remains unresolved.

Specifically, two enantioinduction scenarios, including enantiodetermining HAT and enantiodetermining radical rebound, could account for this stereoselective $C(sp^3)$ -H amination. As described in Figure 1B, in the HAT event, either of the two prochiral C-H bonds (C-H^S and C-H^R) can be cleaved by the Fe nitrene (I), giving rise to two prochiral radical intermediates (II and III), respectively. If the interconversion of the prochiral radicals is slower than the rebound step $(k_1,$ $k_{-1} \ll k_S$, k_R), retention of stereochemistry would be expected in the subsequent radical rebound step. In this scenario, the HAT step would constitute the enantioselectivity-determining step. On the other hand, if the configurational change of this prochiral carbon-centered radical is much faster relative to the rebound step $(k_1, k_{-1} \gg k_S, k_R)$, stereoablation⁸ would take place at this carbon-centered radical. In this case, the subsequent radical rebound would account for the excellent enantioselectivity under the Curtin-Hammett conditions.

Although several computational studies on related P411-catalyzed C(sp³)—H amination processes supported the HAT/radical rebound mechanism, 6e-g,9 the enantioselectivity-determining step and the origin of enantioselectivity in most reactions are still not well understood. It is often assumed that the HAT step is enantioselectivity-determining. 9b,c The enantioselectivity control in the radical rebound step has not been quantitatively investigated by computation or experiment. In particular, the relative rates of C–N bond forming radical rebound and the conformational reorganization of the carbon-centered radical remain elusive. Therefore, it is unclear whether radical rebound has any impact on the enantiose-lectivity. Additionally, the impact of key active site residues on these individual steps in the catalytic cycle is also unexplored.

Here, we report a combined computational and experimental study to shed light on the mechanism and origin of stereoselectivity of this biocatalytic C(sp³)-H amination. To differentiate between the two mechanistic scenarios and gain insights into the origin of stereocontrol, we undertook computational studies using quantum mechanics/molecular mechanics (QM/MM) calculations, classical and ab initio molecular dynamics (MD) simulations. We investigated the reaction free energy profiles and the enantiocontrol of the HAT and the radical rebound steps. We also performed computational studies on the rate of the interconversion between the prochiral carbon-centered radical intermediates. Moreover, deuterium-labeling experiments were performed to support the computational results by quantitatively determining the levels of enantioselectivity in the HAT and radical rebound steps. Finally, the roles of key active site residues on catalytic activity and enantioselectivity were investigated

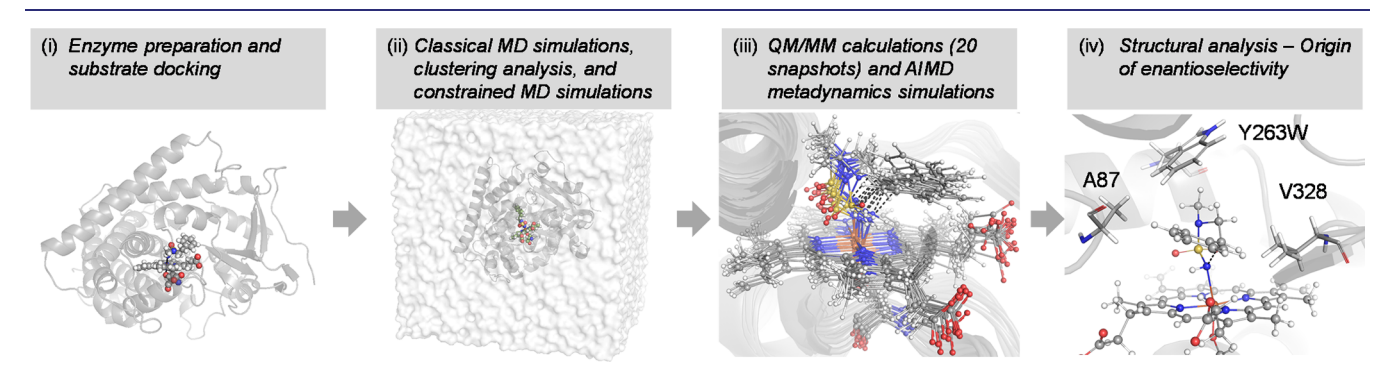


Figure 2. Protocol for computational investigations of asymmetric enzymatic reactions.

computationally and validated experimentally using mutated enzymes generated from site-directed mutagenesis. Collectively, these studies revealed that the enantioselectivity of this enzymatic $C(sp^3)$ -H amination is determined in the radical rebound step, a scenario which is often overlooked in previous

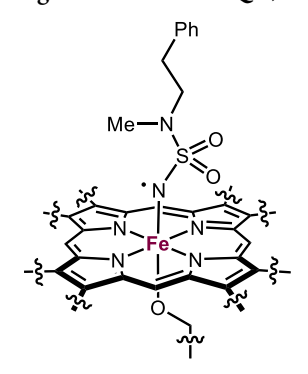
COMPUTATIONAL DETAILS

Classical MD Simulations. To account for the dynamic nature of the protein scaffold, ¹⁰ we implemented the protocol shown in Figure 2 to unravel the reaction mechanism and origin of stereoselectivity in the enzymatic C(sp³)-H amination. The initial geometry of $P411_{Diane2}$ used in the calculations was generated by modifying the X-ray crystal structure of a related P411 enzyme (PDB ID: 5UCW). Eight amino acid residues were mutated using the Mutagenesis tool in PyMOL¹¹ (see Figure S1 for mutated residues). The substrate was then docked into P411_{Diane2} using AutoDock. 12 Classical MD simulations were carried out using the pmemd module¹³ of the GPU-accelerated Amber 16 package.¹⁴ Force field parameters for the Fe nitrene complex were generated using the MCPB. py module 15 with the general Amber force field (gaff), 16 and the Amber ff14SB force field 17 was used for standard residues. After initial equilibration (see the Supporting Information), a 500 ns MD simulation was performed using the isothermal-isobaric ensemble (NPT). Clustering analysis was carried out using the cpptraj module 18 to identify the most populated structure in the last 300 ns of the MD simulation [see Figure S2 for root-mean-square deviation (rmsd) along the 500 ns MD trajectory]. The rmsd of the backbone was used as the distance metrics in the clustering analysis. Conformational samplings of the Fe nitrene intermediate and all the HAT and radical rebound transition states were then carried out using 50 ns of classical MD simulations. For transition states, the breaking and forming bonds were constrained by applying a force constant of 1000 kcal·mol $^{-1}$ ·Å $^{-2}$ in the MD simulations. In the last 20 ns of each MD simulation, snapshots were extracted every 5 ns, giving four structures from each simulation and a total of 20 snapshots. Subsequently, QM/MM calculations were performed using the 20 snapshots as input geometries for each stationary point along the reaction pathway.¹⁹

QM/MM Calculations. The ONIOM method²⁰ implemented in Gaussian 16²¹ was used in all QM/MM calculations. Water molecules and counterions within 5 Å from the enzyme were included in the QM/MM calculations. The QM region includes the Fe-porphine complex, the substrate, and boundary hydrogen atoms, with a total of 66 atoms and a total charge of -1 (Scheme 1). The deprotonated axial serine ligand was used because the calculated pK_{aH} values of a methoxy-ligated Fe(porphine)-nitrene complex (3.07) and a methoxy-ligated Fe(porphine)-NHR complex (1.89) indicate relative high acidity of the protonated serine ligand. The pK_{aH} calculations were performed in an aqueous solution using the computational method described by Smith et al.²² (see the Supporting Information for details). A deprotonated axial ligand was also used in several previous computational studies of P411 enzymes. 6e-g,9a,b,23

For the QM region, the B3LYP²⁴/6-31+G(d)-LANL2DZ-(Fe) level of theory was used in geometry optimization and vibrational frequency calculations, and the B3LYP-D3(BJ)/6-311+G(d,p)-LANL2TZ(f)(Fe) level of theory was used in single-point energy calculations because of its good agreement

Scheme 1. QM Region Used in the QM/MM Calculations



with CCSD(T) benchmark results.^{6e} For the MM region, the same force field parameters from the classical MD simulations discussed above were used. Residues greater than 15 Å away from the QM region were fixed during geometry optimization. The quadratic coupled algorithm²⁵ and the mechanical embedding scheme were used in geometry optimization. Single-point energy calculations were performed with the electronic embedding scheme, which better describes the electrostatic interactions between QM and MM regions.²⁶ Open-shell singlet, triplet, and quintet spin states for each structure were calculated using QM/MM. Wave function stability of the open-shell singlet spin state was confirmed by using the "stable = opt" keyword in Gaussian. Boltzmann-weighted average Gibbs free energies 19a,27 of the 20 snapshots were calculated using

$$\Delta G_{\text{ave}} = -k_{\text{B}} T \ln \left(\frac{1}{n} \sum_{i=1}^{n} \exp \left(\frac{-\Delta G_i}{k_{\text{B}} T} \right) \right)$$
(1)

where n is the number of structures (n = 20), $k_{\rm B}$ is the Boltzmann constant, and T is the temperature (T = 298.15 K). Gibbs free energies computed from individual snapshots (ΔG_i) are provided in the Supporting Information (Table S1).

AIMD Simulations. Ab initio MD (AIMD) simulations were performed using the QUICKSTEP module with the hybrid Gaussian and plane waves (GPW) method²⁸ implemented in the CP2K package.²⁹ Because the entire system is treated using DFT, to reduce computational costs, the enzyme is truncated into a smaller cluster model³⁰ composed of the Fe-porphine complex, the substrate, and side chains of amino acid residues within 5 Å of the substrate based on the QM/MM-optimized geometry of 4_{pro-R} (Scheme 2). The backbone atoms were constrained in the AIMD simulations. The BLYP functional^{24b,31} with D3 dispersion correction³² and the DZVP basis set³³ with Goedecker— Teter-Hutter pseudopotentials³⁴ were used. The plane wave cutoff and the convergence criterion were 280 Ry and 10⁻⁵ au, respectively. Metadynamics simulations³⁵ were carried out at 298 K with a time step of 0.5 fs. The $N^1-C^1-C^2-C^3$ dihedral angle of 4_{pro-R} was used in the metadynamics simulations as a collective variable. The Gibbs free energy profile was obtained using thermodynamic integration.³⁶

EXPERIMENTAL METHODS

Expression of P411 Variants. Escherichia coli [E. cloni Bl21 (DE3)] cells carrying plasmid encoding P411 variant were grown overnight in 4 mL of Luria broth with ampicillin. Preculture (1.5 mL, 5% v/v) was used to inoculate 28.5 mL of hyper broth with ampicillin in a 125 mL Erlenmeyer flask. This culture was incubated at 37 °C,

Scheme 2. Cluster Model Used in the AIMD Metadynamics $Simulations^a$

^aAsterisk symbols indicate fixed carbon atoms on the backbone.

230 rpm for 2 h in a New Brunswick Innova 44R shaker. The culture was then cooled on ice for 20 min and induced with 0.5 mM IPTG and 1.0 mM 5-aminolevulinic acid (final concentrations). Expression was conducted at 22 °C, 150 rpm for 20 h. Cells were then transferred to a 50 mL conical centrifuge tube and pelleted by centrifugation (3000g, 5 min, 4 °C) using an Eppendorf 5910R tabletop centrifuge. The supernatant was removed and the resulting cell pellet was resuspended in M9-N buffer to $\mathrm{OD}_{600} = 30$. An aliquot of this cell suspension (2 mL) was taken to determine the protein concentration by the hemochrome assay after lysis sonication.

Biotransformations Using Whole E. coli Cells. Suspensions of E. coli [E. cloni BL21(DE3)] cells expressing the appropriate P411 variant in M9-N buffer ($OD_{600} = 30$) were kept on ice. In another conical tube, a solution of D-glucose (500 mM in M9-N buffer) was prepared. To a 2 mL vial were added the suspension of E. coli cells expressing P411 (OD₆₀₀ = 30, 345 μ L) and D-glucose (40 μ L of 500 mM stock solution in M9-N buffer). This 2 mL vial was then transferred into an anaerobic chamber, where the azide substrate (15 μL of a 270 mM stock solution in EtOH) was added. The final reaction volume was 400 μ L; final concentrations were 10 mM substrate and 50 mM D-glucose (note: reaction performed with E. coli cells resuspended to $OD_{600} = 30$ indicates that 345 μ L of $OD_{600} = 30$ cells were added, and likewise for other reaction OD_{600} descriptions.) The vials were sealed and shaken in a Corning digital microplate shaker at room temperature and 680 rpm for 12 h. The reaction mixture was then extracted with EtOAc and analyzed by chiral highperformance liquid chromatography (HPLC) using an internal standard.

■ RESULTS AND DISCUSSION

Reaction Mechanism. The Gibbs free energy profile of the P411_{Diane2}-catalyzed C-H amination of sulfamoyl azide substrate 1 obtained from QM/MM calculations is shown in Figure 3 (see Figure S4 in the Supporting Information for QM/MM-optimized structures). The quintet (high spin), triplet (intermediate spin), and open-shell singlet (low spin) spin states of each intermediate and transition state structure were considered in the calculations. Here, only the pathways involving the cleavage of the C-H^S bond of the substrate to form the favored (S)-enantiomer of the product are shown. The cleavage of the C-H^R bond follows the same mechanism (see Figure S5). The origin of enantioselectivity will be discussed in detail in a later section of the article. Our QM/MM calculations reveal that Fe nitrene species 3 has substantial radical character on the nitrogen center, facilitating

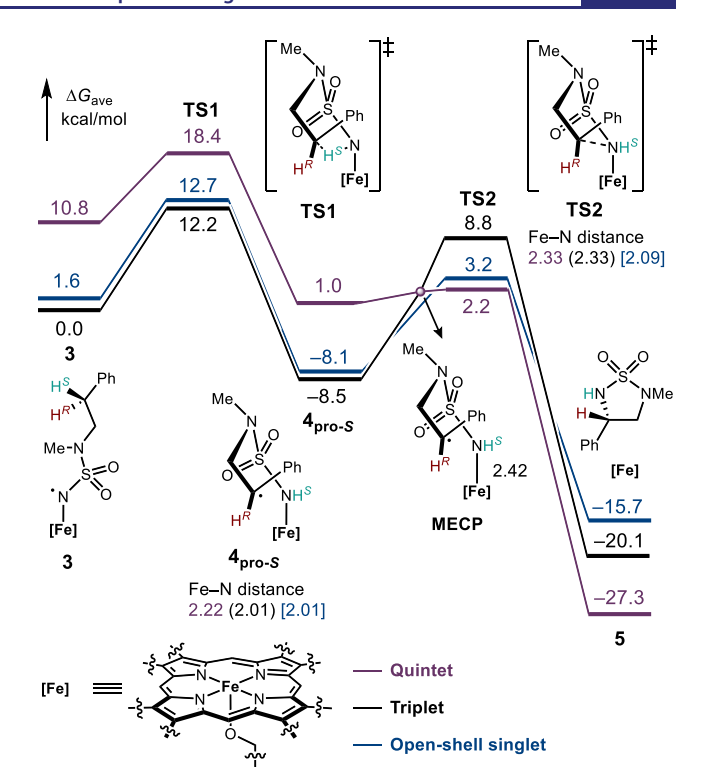


Figure 3. Computed Gibbs free energy profiles of the P411 $_{\rm Diane2}$ -catalyzed C–H amination from QM/MM calculations. Black, blue, and purple values represent bond distances (in Å) of quintet, triplet (in parentheses), and open-shell singlet (in brackets) spin states, respectively.

for the C-H bond activation (see Figure S6 for spin densities of all computed structures). The C-H^S cleavage via TS1 gives rise to the benzylic radical intermediate 4_{pro-S} , where the (Si)face of the benzylic radical points toward the nitrenoid nitrogen. Based on our QM/MM studies, this HAT step is exergonic and irreversible, which is consistent with DFT investigations with a model Fe-porphine complex (Figure S7). In the HAT step, the triplet and open-shell singlet spin states are very similar in energy, whereas the quintet is substantially higher in energy. The similar energy profiles suggest that the HAT step may involve both triplet and singlet spin states, a "two-state reactivity" reminiscent of the HAT step of the native C-H hydroxylation with P450 enzymes, which involves both doublet and quartet states of the active Fe oxo species.³⁷ However, unlike the P450-catalyzed C-H hydroxylation, where the low-spin doublet Fe^{IV}-OH intermediate (compound II) undergoes barrierless radical rebound, both the lowand intermediate-spin intermediates of the Fe^{III}-NHR intermediate 4_{pro-S} require substantial barriers to radical rebound via TS2. Instead, the quintet spin state becomes the most favorable in the radical rebound transition state (TS2), indicating a spin-crossover^{6f,38} event from the triplet and singlet intermediates to the quintet spin state prior to the radical rebound (see Figure S8 for the calculated minimum energy crossing point between the triplet and quintet surfaces).

These computed energy profiles indicated a key difference between the P411_{Diane2}-catalyzed C–H amination and the P450-catalyzed C–H hydroxylation.³⁹ In the P450-catalyzed hydroxylation, low-spin pathways are effectively concerted with ultrashort-lived intermediates, while high-spin pathways are stepwise. By contrast, the P411_{Diane2}-catalyzed C–H amination

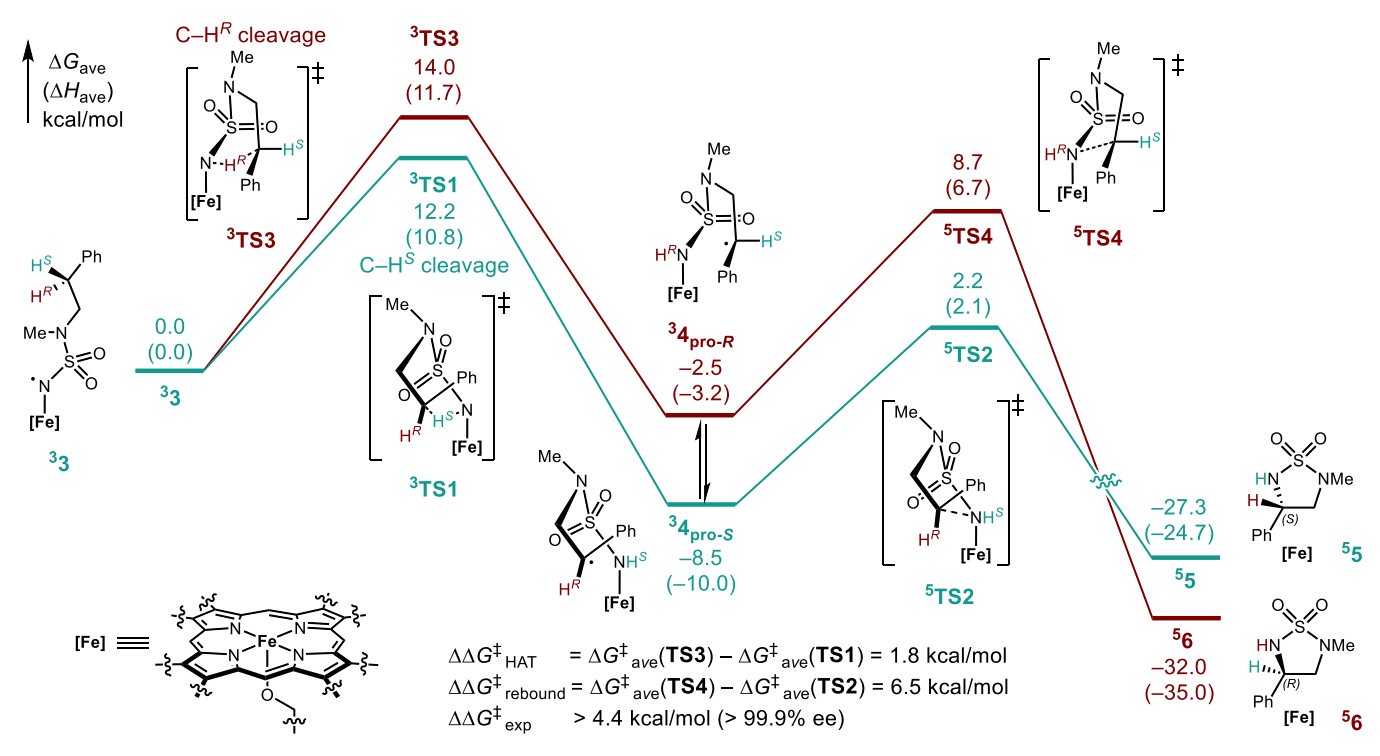


Figure 4. QM/MM-computed free energy profiles of the P411 $_{\rm Diane2}$ -catalyzed amination of two prochiral benzylic C–H bonds in 1. Only the most-stable spin state of each species, denoted by superscript, is reported. $\Delta G_{\rm ave}$ and $\Delta H_{\rm ave}$ values are Boltzmann-weighted Gibbs free energies and enthalpies computed from initial structures taken from 20 MD snapshots. Blue: pathway leading to the major enantiomeric product 2. Red: pathway leading to the minor enantiomeric product ent-2.

favors the stepwise mechanism regardless of whether the singlet or triplet Fe nitrene is involved in HAT. The relatively high barrier in the C-N bond forming radical rebound step is due to the spin-state change from the near-degenerate singlet/ triplet carbon-centered radical 4_{pro-S} to the quintet state in TS2. The radical rebound from singlet and triplet 4_{pro-S} is disfavored due to several factors. First, in the triplet and singlet rebound transition states, ³TS2 and ¹TS2, the Fe-N bond is elongated (2.33 and 2.09 Å, respectively) relative to 4_{pro-S} (2.01 Å), requiring significant distortion. In contrast, the Fe-N bond in quintet ⁵4_{pro-S} is already elongated (2.22 Å). This predistortion of the Fe-N bond facilitates the nitrogen rebound via the quintet state. The elongated Fe-N bond in the quintet 5TS2 reduces the steric repulsions between the secondary benzylic radical and the Fe-porphyrin during radical rebound. Second, the ground state of the product complex is the high-spin quintet Fe(II)-porphyrin 5. This leads to smaller thermodynamic driving force for the radical rebound on the singlet and triplet surfaces compared to that involving the quintet intermediate ⁵4_{pro-S}. Lastly, the fivemembered cyclic transition state TS2 suffers from relatively high ring-strain energy. Based on computed values derived from hypothetical homodesmotic reactions ⁴⁰ (Figure S9), the ring strain energies of the five-membered ring transition state ⁵TS2 and the cyclic amination product 2 are 7.7 and 5.1 kcal/ mol, respectively. Therefore, the ring strain energy of the cyclization transition state makes the intramolecular C-N rebound slower than the corresponding intermolecular process. 6f,g,9b,c Taken together, the QM/MM-computed reaction energy profiles revealed an unusual mechanism with a high-barrier radical rebound, indicating relatively long lifetimes of the carbon-centered radical intermediates, which

may lead to the ablation of stereochemistry prior to radical rebound.

Enantioselectivity in the HAT and Radical Rebound **Steps.** Because the high radical rebound barrier shown above indicates that either the HAT or the radical rebound step can be enantioselectivity-determining, we computed the enantioselectivity in both steps in the amination of the two prochiral benzylic C-H bonds in 1 (Figure 4). From the Fe nitrene species 3, HAT with the $C-H^S$ (TS1) and $C-H^R$ (TS3) bonds require activation free energies of 12.2 and 14.0 kcal/ mol, respectively. After the formation of the prochiral benzylic radical intermediates 4_{pro-R} and 4_{pro-S}, subsequent C-N bond forming radical rebound takes place via quintet transition states, TS2 and TS4, to form the two enantiomers of the amination product. The computed activation free energy difference $(\Delta \Delta G^{\ddagger})$ between radical rebound transition states TS2 and TS4 is 6.5 kcal/mol, much higher than the moderate $\Delta\Delta G^{\dagger}$ of the HAT step, which is only 1.8 kcal/mol.

The computed energy profiles have some interesting implications on the enantiocontrol of the asymmetric amination. Although the HAT step is exergonic and irreversible, the relatively high barriers to radical rebound suggest that the rate of interconversion between benzylic radical intermediates $4_{\text{pro-R}}$ and $4_{\text{pro-S}}$ may be faster than the C-N bond forming radical rebound. This scenario is reminiscent of the Curtin-Hammett principle, where the enantioselectivity is only affected by the energy difference between the radical rebound transition states, **TS2** and **TS4**. Additionally, the computed $\Delta\Delta G^{\ddagger}$ for HAT (1.8 kcal/mol) corresponds to 91% ee, much lower than the experimentally observed enantioselectivity (>99.9% ee). On the other hand, the high enantioselectivity in the radical rebound step ($\Delta\Delta G^{\ddagger}$ = 6.5 kcal/mol, which corresponds to >99.9% ee) is consistent

with the high levels of enantioselectivity observed in the experiment.

Deuterium-Labeling Experiments. Our QM/MM calculations revealed an unusual enantioinduction mechanism, wherein the HAT step is moderately enantioselective and the nitrogen-rebound step is highly enantioselective. To further shed light on the enantioselectivity-determining step in this intramolecular C–H amination, we prepared a set of enantiopure monodeutero, monoprotio substrates and subjected them to the enzymatic reaction conditions (Figure 5A).

(A) Deuterium-labeling experiments

KIE and enzyme enantiocontrol both favor C–H cleavage: $\Delta G_{\text{KIE}} + \Delta G_{\text{enantioselectivity}} = \Delta G^{\ddagger}_{\text{H/D}}(\text{HAT-}(R)\text{-1-}d_1) \\ = -\text{RTIn}(k_{\text{H}}/k_{\text{D}}) = -1.87 \text{ kcal/mol}$

(B) Dissecting the KIE and enzyme enantioinduction effects

- ΔG_{KIE} = -0.73 kcal/mol implications
 - HAT step is irreversible
- ∆G_{enantioselectivity} = −1.14 kcal/mol
- HAT step is moderately
 enantioselective.
- high ee for both Eqs. 1 and 2
- Enantioselectivity is not determined in the HAT step.

Figure 5. Enantioselectivity-determining step in the P411 $_{\rm Diane2}$ -catalyzed C—H amination identified by deuterium-labeling experiments. Reactions were carried out using whole *E. coli* cells harboring P411 $_{\rm Diane2}$. Product distribution and enantioselectivity were provided in the figure. <10% Deuterium on the N atom was observed by $^{\rm 1}$ H NMR spectroscopy, presumably due to proton exchange with H₂O of the reaction buffer.

When (R)-1- d_1 was applied, the biocatalytic C–H amination furnished the product with >99% ee, and the 2- d_1 /2 ratio was determined to be 96:4 on the basis of ¹H NMR analysis. When (S)-1- d_1 was applied, this biocatalytic amination reaction still furnished the same enantiomeric product with >99% ee, and the 2/2- d_1 ratio was found to be 67:33.

Quantitative activation free energy analysis of these reactions was next performed (Figure 5B. See Figures S10 and S11 for detailed calculations). Based on our QM/MM-computed energy profiles with evolved P411_{Diane2} (Figure 4) and DFT calculations on a model complex (Figure S7), the HAT step in this C–H amination is irreversible. Thus, the $\mathbf{2/2}$ - d_1 ratio, that is, $\Delta\Delta G^{\ddagger}_{\mathrm{H/D}}(\mathrm{HAT})$, is controlled by two energy terms, including ΔG_{KIE} , which reflects the kinetic isotope effect (KIE) in the HAT step, and $\Delta G_{\mathrm{enantioselectivity}}$, which reflects the

enzyme-induced enantioselectivity in the HAT event with the non-deuterated substrate. With (R)-1- d_1 as the substrate, both the KIE and the enzymatic stereocontrol favor the abstraction of the pro-(S)-H, thus leading to a higher $2-d_1/2$ ratio. On the other hand, when $(S)-1-d_1$ was applied, enzymatic stereocontrol overrides the inherent KIE effect, resulting in a lower $2/2-d_1$ ratio. Activation free energy analysis allowed us to dissect the two effects, and the two energy terms of ΔG_{KIE} and $\Delta G_{
m enantios electivity}$ were determined to be -0.73 and -1.14 kcal/ mol, respectively. This ΔG_{KIE} value corresponds to a $k_{\text{H}}/k_{\text{D}}$ of 3.4. This KIE is consistent with previously measured KIEs with related enzymatic intramolecular C-H amination processes. 6b,l The primary intramolecular KIE suggests an irreversible HAT step, which is consistent with the computed reaction energy profiles. Moreover, the small value of $\Delta G_{\text{enantioselectivity}}$ for the HAT step corresponds to an enantiomeric ratio (e.r.) of 87:13 (74% ee), clearly showing that the HAT step with P411_{Diane2} is only moderately enantioselective, and the very high level of product enantiopurity was controlled by the radical rebound step. Therefore, these results suggest that the benzylic radical is relatively long-lived, and the excellent enantioselectivity observed in this enzymatic C-H amination is likely controlled by the C-N bond-forming radical rebound step.

Stereoablation after HAT via Conformational Change of Benzylic Radical Species. The experimental and computational results discussed above indicate that although HAT is irreversible, it is not enantioselectivity-determining. This means the prochiral benzylic radical intermediates 4_{pro-R} and 4_{pro-S} must undergo rapid interconversion before the radical rebound. This mechanistic scenario is not well understood for radical-mediated enzymatic reactions, particularly new-to-nature enzymatic reactions, considering the short lifetime of radical intermediates.

In order to investigate the rate of the interconversion between benzylic radical intermediates $\mathbf{4}_{pro\text{-}R}$ and $\mathbf{4}_{pro\text{-}S}$ via conformational reorganization, classical MD and AIMD simulations were carried out. 41 Using the QM/MM-optimized structure of 4_{pro-R} as the starting geometry, a 500 ns classical MD simulation was performed. Within the first 6.5 ns of the MD simulation, a snapshot with geometry akin to 4_{pro-S} was obtained (see Figure S12). The rotations about the S-N¹ and C^1-C^2 bonds (Figure 6A,B) occur at approximately the same time, from 6.0 to 6.3 ns (see Figure S13 for rotation about the N^1-C^1 bond). This process allows the bulky Ph group on the substrate to point toward the same direction without clashing with the Fe-porphyrin. Throughout the 500 ns classical MD simulation, frequent rotations about the S-N1 and C1-C2 bonds were observed (see Figure S14). These results suggest that within the enzyme's active site, the benzylic radical is conformationally flexible and can rapidly rotate to expose either prochiral face of the carbon-centered radical toward Fe^{III}-NHR prior to the C-N bond forming radical rebound.

Next, we performed AIMD metadynamics simulations to quantitively determine the Gibbs free energy barrier to the isomerization of the benzylic radical intermediates. The AIMD simulations suggest that the transformation of $4_{\text{pro-R}}$ to $4_{\text{pro-S}}$ is facile, with a low barrier of 3.6 kcal/mol with respect to $4_{\text{pro-R}}$ (Figure 6C). This result is consistent with the rapid conformational change observed in the classical MD simulations. Most importantly, this conformational change from $4_{\text{pro-R}}$ to $4_{\text{pro-S}}$ occurs at a time scale faster than the C–N bond-forming radical rebound, highlighting the essential role of

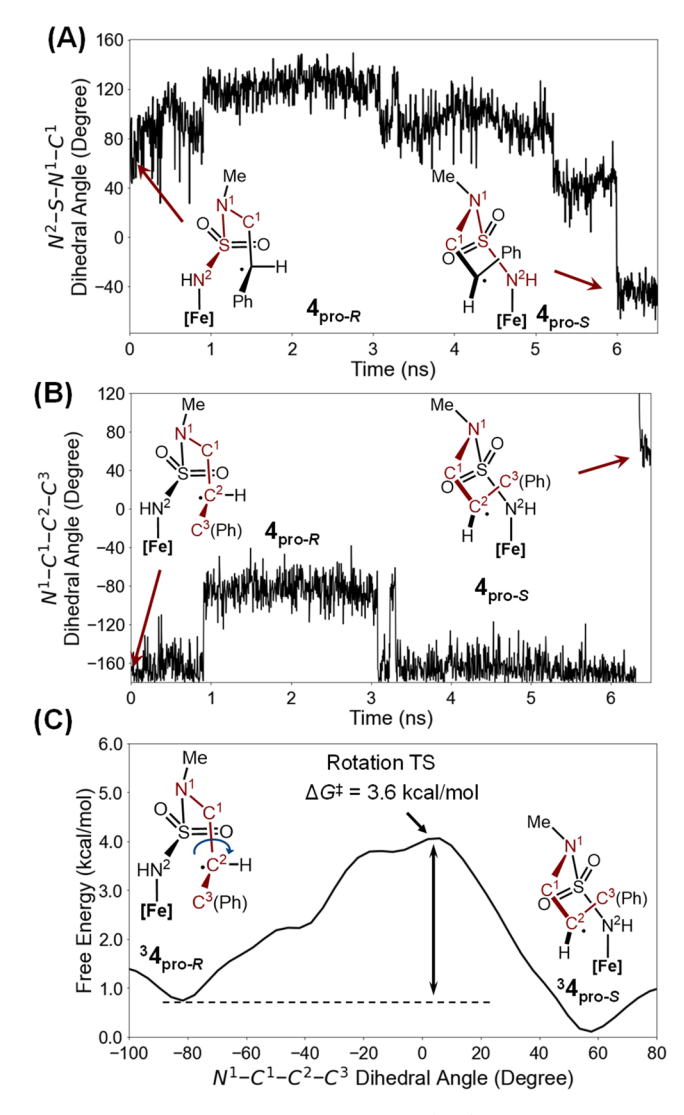


Figure 6. Isomerization of $\mathbf{4_{pro-R}}$ to $\mathbf{4_{pro-S}}$. (A,B) Rotations about S-N¹ (A) and C¹-C² (B) bonds in the first 6.5 ns of a 500 ns classical MD simulation starting from $\mathbf{4_{pro-R}}$. (C): Free energy profile of the isomerization from AIMD metadynamics simulation of a cluster model of ${}^{3}\mathbf{4_{pro-R}}$ using the N¹-C¹-C²-C³ dihedral angle as a collective variable.

radical rebound in determining the enantioselectivity of this enzymatic C–H amination.⁴²

Origin of Enantioselectivity and the Roles of Key Residues. The QM/MM-optimized structures of intermediates and transition states in the C-H amination pathways are shown in Figure 7. In all structures, $C-H/\pi$ or π/π interactions between the substrate and the W263 residue, a key mutation previously introduced during the directed evolution of P411_{Diane2}, are observed. This indicates that W263 plays an essential role in enhancing substrate binding and stabilizing intermediates and both HAT and radical rebound transition states. With the $C-H/\pi$ interaction with W263 and a steric effect of A87, the orientation of the substrate is constrained, pointing the Ph group on the substrate toward V328, a key residue for enantioinduction (vide infra).

In the transition state stereoisomers leading to the opposite enantiomeric products, the benzylic C–H bonds in TS1 and TS3 and the benzylic radical in TS2 and TS4 approach from the opposite faces of the Fe nitrene or Fe^{III}–NHR complex. In

transition states **TS3** and **TS4**, the benzyl group is placed close to V328, leading to steric repulsions between these two groups, whereas in **TS1** and **TS2**, the benzyl group approaches from the opposite side of V328, and thus, the steric repulsion is diminished. Although **TS3** and **TS4** are both destabilized by steric repulsions with V328, the magnitude of steric effect is different—the Ph group is placed much closer to V328 in the radical rebound transition state **TS4** $[d(H\cdots H)=2.14 \text{ Å}]$ because of the shorter distance between the benzylic carbon and the Fe–porphyrin (2.33 Å) than that in **TS3**. The stronger steric repulsions that destabilize **TS4** lead to the greater enantioselectivity in the radical rebound step $(\Delta\Delta G^{\ddagger}_{\text{rebound}}=6.5 \text{ kcal/mol})$ compared to that in the HAT step $(\Delta\Delta G^{\ddagger}_{\text{HAT}}=1.8 \text{ kcal/mol})$.

To validate the computationally revealed roles of key residues, such as W263, V328, and A87, we carried out sitedirected mutagenesis and tested the catalytic activity and enantioselectivity of these P411_{Diane2} variants (Tables 1 and S4). We found that mutations W263A and W263F did not affect the enantioselectivity but substantially reduced the enzyme activity (Table 1, entries 1-3). This finding is consistent with the stabilization effect of W263 observed from QM/MM calculations. The $P411_{Diane2}\ A87V$ and A87Lvariants also led to lower yields without impacting enantioselectivity (entries 4-5). This suggests that a larger residue 87 may hinder substrate binding and decrease conversion without altering the mode of enantioinduction. We further validated the role of V328 by evaluating the enantioselectivity of P411_{Diane2} V328A generated by sitedirected mutagenesis. Indeed, mutant P411_{Diane2} V328A provided product 2 with 97% ee and lower activity, suggesting a larger residue at 328 is needed for enantiocontrol (entry 6). Furthermore, double mutants P411_{Diane2} V328A A87V and P411_{Diane2} V328A A87L were generated and found to furnish further decreased enantioselectivity (81 and 55% ee, respectively, entries 7-8). Our QM/MM calculations using the V328A A87V variant indeed showed a decreased enantioselectivity in the radical rebound step ($\Delta \Delta G^{\ddagger} = 1.7$ kcal/mol, Figure S17) due to reduced steric repulsions between the substrate and residue 328. These results are consistent with our computational model and demonstrate the importance of residues 328 and 87 in crafting a substrate binding pocket for excellent enantiodifferentiation.

CONCLUSIONS

Using a combined QM/MM and experimental approach, we investigated the mechanism and origin of enantioselectivity of the recently developed biocatalytic asymmetric $C(sp^3)$ -H amination process. This C-H amination was found to occur via an irreversible HAT step and a C-N bond-forming radical rebound step. Contrary to previous understanding on enantioinduction mechanisms, we showed that radical rebound, rather than HAT, is enantioselectivity-determining in this biocatalytic intramolecular C-H amination. Our QM/ MM calculations indicated that the radical rebound is relatively slow due to the spin-state change and ring strain in the intramolecular cyclization transition state. Classical and AIMD simulations suggested that the carbon-centered radical undergoes much faster conformational change, allowing for stereoablation at the carbon-centered radical intermediate. Therefore, under the Curtin-Hammett conditions, the enantioselectivity is determined in the radical rebound step. The QM/ MM-computed activation free energy differences between the

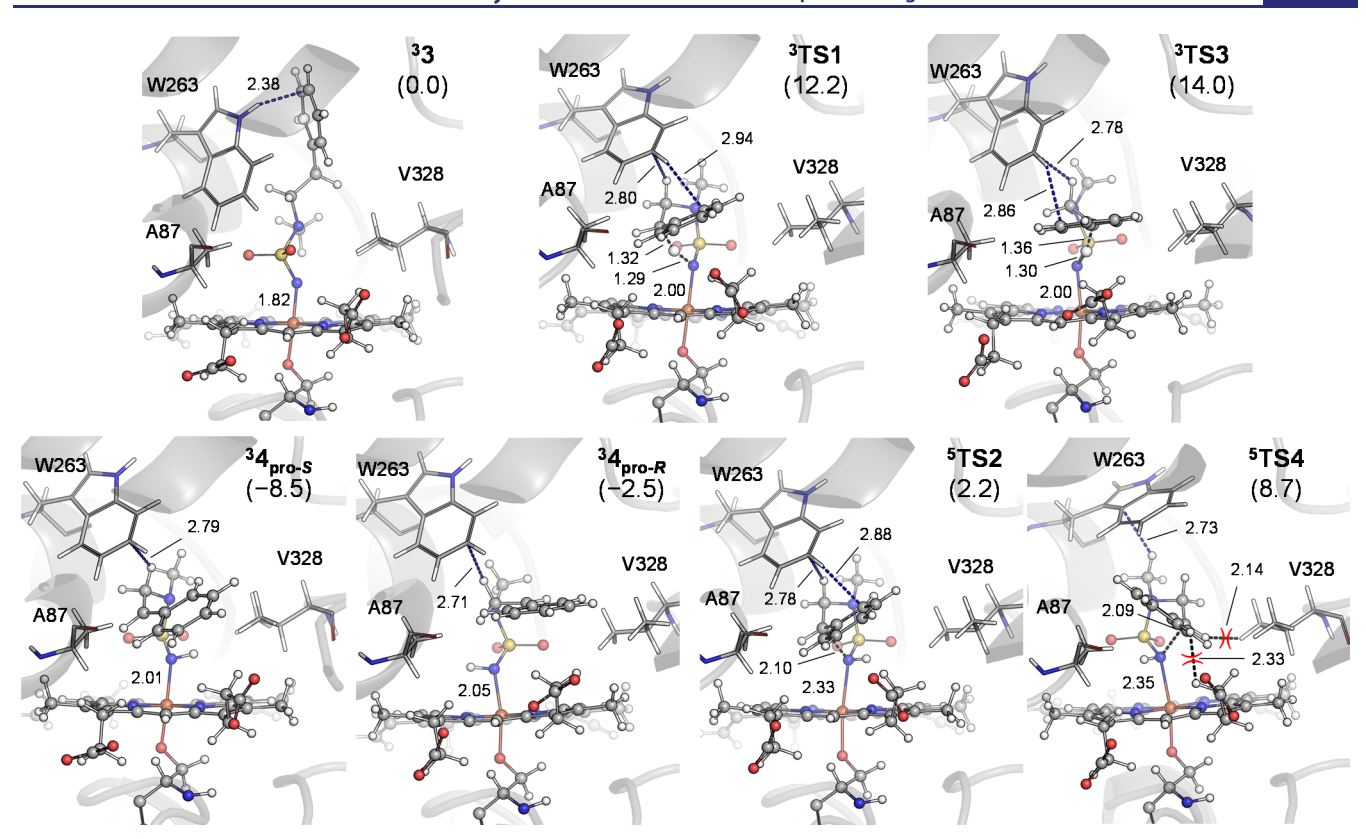


Figure 7. QM/MM-optimized lowest-energy structures of the intermediates and transition states in the P411_{Diane2}-catalyzed asymmetric amination of secondary $C(sp^3)$ -H bond in 1. Boltzmann-weighted Gibbs free energies (in parentheses, kcal/mol) are relative to Fe nitrene species ³3. Blue dashed lines represent C-H/ π interactions, measured by the shortest distance between the hydrogen atom and a carbon atom on the aromatic ring. Distances are in Å.

Table 1. Effects of Key Residues W263, A87, and V328 on Activity and Enantioselectivity of Enzyme Variants Generated by Site-Directed Mutagenesis

entry	enzyme mutant	yield (%) ^a	TTN	ee (%) ^a
1	P411 _{Diane2}	81 ± 1	2460 ± 20	>99
2	P411 _{Diane2} W263A	1.4 ± 0	40 ± 10	>99
3	P411 _{Diane2} W263F	24 ± 1	850 ± 20	>99
4	$P411_{Diane2} A87V$	40 ± 4	1100 ± 100	>99
5	P411 _{Diane2} A87L	8 ± 1	450 ± 70	>99
6	P411 _{Diane2} V328A	59 ± 3	1690 ± 60	97
7	$P411_{Diane2}\ V328A\ A87V$	18 ± 2	510 ± 60	81
8	P411 _{Diane2} V328A A87L	3 ± 0	150 ± 4	55

"Yields and ee's were determined by HPLC analysis. Reactions were carried out using whole $E.\ coli$ cells harboring P411 $_{\rm Diane2}$ mutants.

two stereoisomeric pathways indicated a moderate level of stereoselectivity in the HAT step ($\Delta\Delta G^{\ddagger}=1.8~\text{kcal/mol}$) and an excellent level of enantioinduction ($\Delta\Delta G^{\ddagger}=6.5~\text{kcal/mol}$) at the radical rebound stage that can account for the high levels of enantioselectivity observed in the experiment. These computational findings are corroborated by experimental results employing enantiopure and deuterium-labeled substates, which also indicated moderate enantioselectivity in an irreversible C–H cleavage event, and thus, the excellent

enantioselectivity of the overall amination must be controlled in the subsequent radical rebound step. The roles of several key active site residues, including W263, A87, and V328, in confining substrate orientation and manifesting enantioinduction via steric effects, have been demonstrated computationally and validated experimentally by evaluating the activity and enantioselectivity of enzyme variants generated by site-directed mutagenesis. Together, this study highlights an unusual enantioinduction mechanism in metalloenzyme-catalyzed asymmetric transformations involving radical intermediates. We expect that these insights will guide the further development of stereoselective new-to-nature biocatalytic reactions using a radical mechanism.

ASSOCIATED CONTENT

5 Supporting Information

The Supporting Information is available free of charge at https://pubs.acs.org/doi/10.1021/jacs.2c02283.

Additional computational and experimental results, Cartesian coordinates, and energies of DFT-computed structures (PDF)

Cartesian coordinates of the lowest-energy structures of all intermediates and transition states from QM/MM calculations (ZIP)

AUTHOR INFORMATION

Corresponding Authors

Yang Yang – Department of Chemistry and Biochemistry and Biomolecular Science and Engineering (BMSE) Program, University of California, Santa Barbara, California 93106, *United States*; orcid.org/0000-0002-4956-2034; Email: yang@chem.ucsb.edu

Peng Liu – Department of Chemistry, University of Pittsburgh, Pittsburgh, Pennsylvania 15260, United States; o orcid.org/ 0000-0002-8188-632X; Email: pengliu@pitt.edu

Authors

Binh Khanh Mai - Department of Chemistry, University of Pittsburgh, Pittsburgh, Pennsylvania 15260, United States; orcid.org/0000-0001-8487-1417

Natalia M. Neris - Department of Chemistry and Biochemistry, University of California, Santa Barbara, California 93106, United States

Complete contact information is available at: https://pubs.acs.org/10.1021/jacs.2c02283

Author Contributions

The manuscript was written through the contributions of all authors.

Notes

The authors declare no competing financial interest.

ACKNOWLEDGMENTS

We acknowledge the NIH (R35GM128779 for P.L.) and the University of California, Santa Barbara (Y.Y.) for financial support. We are grateful to Prof. Frances Arnold (California Institute of Technology) for her support. We thank Drs. Leonardo Bernasconi and Xiaotian Qi for helpful discussions. Computational calculations were carried out at the Center for Research Computing at the University of Pittsburgh and the Extreme Science and Engineering Discovery Environment (XSEDE) supported by the National Science Foundation grant number ACI-1548562. We acknowledge the BioPACIFIC MIP (NSF Materials Innovation Platform, DMR-1933487) at UCSB for access to instrumentation and the NSF MRSEC program (seed grant to Y.Y. through DMR-1720256) for partial support.

REFERENCES

- (1) (a) Davies, H. M. L.; Manning, J. R. Catalytic C-H functionalization by metal carbenoid and nitrenoid insertion. Nature 2008, 451, 417-424. (b) Gutekunst, W. R.; Baran, P. S. functionalization logic in total synthesis. Chem. Soc. Rev. 2011, 40, 1976-1991. (c) Lu, H.; Zhang, X. P. Catalytic C-H functionalization by metalloporphyrins: recent developments and future directions. Chem. Soc. Rev. 2011, 40, 1899-1909. (d) Che, C.-M.; Lo, V. K.-Y.; Zhou, C.-Y.; Huang, J.-S. Selective functionalisation of saturated C-H bonds with metalloporphyrin catalysts. Chem. Soc. Rev. 2011, 40, 1950-1975. (e) Hartwig, J. F.; Larsen, M. A. Undirected, homogeneous C-H bond functionalization: Challenges and opportunities. ACS Cent. Sci. 2016, 2, 281-292. (f) Gandeepan, P.; Müller, T.; Zell, D.; Cera, G.; Warratz, S.; Ackermann, L. 3d Transition metals for C-H activation. Chem. Rev. 2019, 119, 2192-2452. (g) Liu, Y.; You, T.; Wang, H.-X.; Tang, Z.; Zhou, C.-Y.; Che, C.-M. Iron- and cobalt-catalyzed C(sp³)-H bond functionalization reactions and their application in organic synthesis. Chem. Soc. Rev. 2020, 49, 5310-5358.
- (2) (a) Newton, C. G.; Wang, S.-G.; Oliveira, C. C.; Cramer, N. Catalytic enantioselective transformations involving C-H bond cleavage by transition-metal complexes. Chem. Rev. 2017, 117, 8908-8976. (b) Saint-Denis, T. G.; Zhu, R. Y.; Chen, G.; Wu, Q. F.; Yu, J. Q. Enantioselective C(sp³)-H bond activation by chiral transition metal catalysts. Science 2018, 359, No. eaao4798.
- (3) (a) Müller, P.; Fruit, C. Enantioselective catalytic aziridinations and asymmetric nitrene insertions into CH bonds. Chem. Rev. 2003,

- 103, 2905-2920. (b) Roizen, J. L.; Harvey, M. E.; Du Bois, J. Metalcatalyzed nitrogen-atom transfer methods for the oxidation of aliphatic C-H bonds. Acc. Chem. Res. 2012, 45, 911-922. (c) Alderson, J. M.; Corbin, J. R.; Schomaker, J. M. Tunable, chemo- and site-selective nitrene transfer reactions through the rational design of silver(I) catalysts. Acc. Chem. Res. 2017, 50, 2147-2158. (d) Park, Y.; Kim, Y.; Chang, S. Transition metal-catalyzed C-H amination: Scope, mechanism, and applications. Chem. Rev. 2017,
- (4) (a) Lewis, J. C.; Coelho, P. S.; Arnold, F. H. Enzymatic functionalization of carbon-hydrogen bonds. Chem. Soc. Rev. 2011, 40, 2003-2021. (b) Li, F.; Zhang, X.; Renata, H. Enzymatic C-H functionalizations for natural product synthesis. Curr. Opin. Chem. Biol. 2019, 49, 25-32. (c) Zhang, R. K.; Huang, X.; Arnold, F. H. Selective C-H bond functionalization with engineered heme proteins: New tools to generate complexity. Curr. Opin. Chem. Biol. 2019, 49, 67-75. (d) Ren, X.; Fasan, R. Engineered and artificial metalloenzymes for selective C-H functionalization. Curr. Opin. Green Sustainable Chem. 2021, 31, 100494.

(5) (a) Brandenberg, O. F.; Fasan, R.; Arnold, F. H. Exploiting and

engineering hemoproteins for abiological carbene and nitrene transfer reactions. Curr. Opin. Biotechnol. 2017, 47, 102-111. (b) Natoli, S. N.; Hartwig, J. F. Noble-metal substitution in hemoproteins: An emerging strategy for abiological catalysis. Acc. Chem. Res. 2019, 52, 326-335. (c) Yang, Y.; Arnold, F. H. Navigating the unnatural reaction space: Directed evolution of heme proteins for selective carbene and nitrene transfer. Acc. Chem. Res. 2021, 54, 1209-1225. (6) (a) McIntosh, J. A.; Coelho, P. S.; Farwell, C. C.; Wang, Z. J.; Lewis, J. C.; Brown, T. R.; Arnold, F. H. Enantioselective intramolecular C-H amination catalyzed by engineered cytochrome P450 enzymes in vitro and in vivo. Angew. Chem., Int. Ed. 2013, 52, 9309-9312. (b) Hyster, T. K.; Farwell, C. C.; Buller, A. R.; McIntosh, J. A.; Arnold, F. H. Enzyme-controlled nitrogen-atom transfer enables regiodivergent C-H amination. J. Am. Chem. Soc. 2014, 136, 15505-15508. (c) Prier, C. K.; Zhang, R. K.; Buller, A. R.; Brinkmann-Chen, S.; Arnold, F. H. Enantioselective, intermolecular benzylic C-H amination catalysed by an engineered iron-haem enzyme. Nat. Chem. 2017, 9, 629-634. (d) Jia, Z.-J.; Gao, S.; Arnold, F. H. Enzymatic primary amination of benzylic and allylic $C(sp^3)$ -H bonds. J. Am. Chem. Soc. 2020, 142, 10279-10283. (e) Yang, Y.; Cho, I.; Qi, X.; Liu, P.; Arnold, F. H. An enzymatic platform for the asymmetric amination of primary, secondary and tertiary $C(sp^3)$ -H bonds. Nat. Chem. 2019, 11, 987-993. (f) Athavale, S. V.; Gao, S.; Liu, Z.; Mallojjala, S. C.; Hirschi, J. S.; Arnold, F. H. Biocatalytic, intermolecular C-H bond functionalization for the synthesis of enantioenriched amides. Angew. Chem., Int. Ed. 2021, 60, 24864-24869. (g) Liu, Z.; Qin, Z.-Y.; Zhu, L.; Athavale, S. V.; Sengupta, A.; Jia, Z.-J.; Garcia-Borràs, M.; Houk, K. N.; Arnold, F. H. An enzymatic platform for primary amination of 1-aryl-2-alkyl alkynes. J. Am. Chem. Soc. 2022, 144, 80-85. (h) Singh, R.; Kolev, J. N.; Sutera, P. A.; Fasan, R. Enzymatic $C(sp^3)$ -H amination: P450-catalyzed conversion of carbonazidates into oxazolidinones. ACS Catal. 2015, 5, 1685-1691. (i) Singh, R.; Bordeaux, M.; Fasan, R. P450-catalyzed intramolecular sp³ C-H amination with arylsulfonyl azide substrates. ACS Catal. 2014, 4, 546-552. (j) Dydio, P.; Key, H. M.; Hayashi, H.; Clark, D. S.; Hartwig, J. F. Chemoselective, enzymatic C-H bond amination catalyzed by a cytochrome P450 containing an Ir(Me)-PIX cofactor. J. Am. Chem. Soc. 2017, 139, 1750-1753. (k) Moore, E. J.; Fasan, R. Effect of proximal ligand substitutions on the carbene and nitrene transferase activity of myoglobin. Tetrahedron 2019, 75, 2357-2363. (1) Steck, V.; Kolev, J. N.; Ren, X.; Fasan, R. Mechanismguided design and discovery of efficient cytochrome P450-derived C-H amination biocatalysts. J. Am. Chem. Soc. 2020, 142, 10343-10357. (7) For related intramolecular nitrene transfer processes using transition metal catalysts, see: (a) Lu, H.; Jiang, H.; Wojtas, L.; Zhang, X. P. Selective intramolecular C-H amination through the metalloradical activation of azides: synthesis of 1,3-diamines under neutral and nonoxidative conditions. Angew. Chem., Int. Ed. 2010, 49, 10192-

10196. (b) Li, C.; Lang, K.; Lu, H.; Hu, Y.; Cui, X.; Wojtas, L.; Zhang,

- X. P. Catalytic radical process for enantioselective amination of C(sp³)-H bonds. Angew. Chem., Int. Ed. **2018**, 57, 16837-16841. (c) Lang, K.; Torker, S.; Wojtas, L.; Zhang, X. P. Asymmetric induction and enantiodivergence in catalytic radical C-H amination via enantiodifferentiative H-atom abstraction and stereoretentive radical substitution. J. Am. Chem. Soc. 2019, 141, 12388-12396. (d) Hu, Y.; Lang, K.; Li, C.; Gill, J. B.; Kim, I.; Lu, H.; Fields, K. B.; Marshall, M.; Cheng, Q.; Cui, X.; Wojtas, L.; Zhang, X. P. Enantioselective radical construction of 5-membered cyclic sulfonamides by metalloradical C-H amination. J. Am. Chem. Soc. 2019, 141, 18160-18169. (e) Lang, K.; Li, C.; Kim, I.; Zhang, X. P. Enantioconvergent amination of racemic tertiary C-H bonds. J. Am. Chem. Soc. 2020, 142, 20902-20911. (f) Hong, S. Y.; Park, Y.; Hwang, Y.; Kim, Y. B.; Baik, M. H.; Chang, S. Selective formation of γ -lactams via C-H amidation enabled by tailored iridium catalysts. Science 2018, 359, 1016-1021. (g) Wang, H.; Park, Y.; Bai, Z.; Chang, S.; He, G.; Chen, G. Iridium-catalyzed enantioselective C(sp³)-H amidation controlled by attractive noncovalent interactions. J. Am. Chem. Soc. 2019, 141, 7194-7201. (h) Park, Y.; Chang, S. Asymmetric formation of γ -lactams via C-H amidation enabled by chiral hydrogen-bond-donor catalysts. Nat. Catal. 2019, 2, 219-227. (i) Lee, E.; Hwang, Y.; Kim, Y. B.; Kim, D.; Chang, S. Enantioselective access to spirolactams via nitrenoid transfer enabled by enhanced noncovalent interactions. J. Am. Chem. Soc. 2021, 143, 6363-6369. (j) Hennessy, E. T.; Betley, T. A. Complex Nheterocycle synthesis via iron-catalyzed, direct C-H bond amination. Science 2013, 340, 591-595. (k) Iovan, D. A.; Wilding, M. J. T.; Baek, Y.; Hennessy, E. T.; Betley, T. A. Diastereoselective C-H bond amination for disubstituted pyrrolidines. Angew. Chem., Int. Ed. 2017, 56, 15599-15602. (1) Dong, Y.; Clarke, R. M.; Porter, G. J.; Betley, T. A. Efficient C-H amination catalysis using nickel-dipyrrin complexes. J. Am. Chem. Soc. 2020, 142, 10996-11005. (m) Dong, Y.; Lund, C. J.; Porter, G. J.; Clarke, R. M.; Zheng, S.-L.; Cundari, T. R.; Betley, T. A. Enantioselective C-H amination catalyzed by nickel iminyl complexes supported by anionic bisoxazoline (BOX) ligands. J. Am. Chem. Soc. 2021, 143, 817-829. (n) Ju, M.; Zerull, E. E.; Roberts, J. M.; Huang, M.; Guzei, I. A.; Schomaker, J. M. Silver-catalyzed enantioselective propargylic C-H bond amination through rational ligand design. J. Am. Chem. Soc. 2020, 142, 12930-12936.
- (8) Bhat, V.; Welin, E. R.; Guo, X.; Stoltz, B. M. Advances in stereoconvergent catalysis from 2005 to 2015: Transition-metalmediated stereoablative reactions, dynamic kinetic resolutions, and dynamic kinetic asymmetric transformations. Chem. Rev. 2017, 117,
- (9) (a) Li, X.; Dong, L.; Liu, Y. Theoretical study of iron porphyrin nitrene: Formation mechanism, electronic nature, and intermolecular C-H amination. Inorg. Chem. 2020, 59, 1622-1632. (b) Wang, J.; Gao, H.; Yang, L.; Gao, Y. Q. Role of engineered iron-haem enzyme in reactivity and stereoselectivity of intermolecular benzylic C-H bond amination. ACS Catal. 2020, 10, 5318-5327. (c) Kalita, S.; Shaik, S.; Dubey, K. D. MD simulations and QM/MM calculations reveal the key mechanistic elements which are responsible for the efficient C-H amination reaction performed by a bioengineered P450 enzyme. Chem. Sci. 2021, 12, 14507-14518.
- (10) (a) Campbell, E.; Kaltenbach, M.; Correy, G. J.; Carr, P. D.; Porebski, B. T.; Livingstone, E. K.; Afriat-Jurnou, L.; Buckle, A. M.; Weik, M.; Hollfelder, F.; Tokuriki, N.; Jackson, C. J. The role of protein dynamics in the evolution of new enzyme function. Nat. Chem. Biol. 2016, 12, 944-950. (b) Biel, J. T.; Thompson, M. C.; Cunningham, C. N.; Corn, J. E.; Fraser, J. S. Flexibility and design: Conformational heterogeneity along the evolutionary trajectory of a redesigned ubiquitin. Structure 2017, 25, 739-749.e3. (c) Buller, A. R.; van Roye, P.; Cahn, J. K. B.; Scheele, R. A.; Herger, M.; Arnold, F. H. Directed evolution mimics allosteric activation by stepwise tuning of the conformational ensemble. J. Am. Chem. Soc. 2018, 140, 7256-
- (11) The PyMOL Molecular Graphics System, 2.5.0; Schrödinger, LLC.

- (12) Morris, G. M.; Huey, R.; Lindstrom, W.; Sanner, M. F.; Belew, R. K.; Goodsell, D. S.; Olson, A. J. AutoDockTools4 Automated docking with selective receptor flexibility. J. Comput. Chem. 2009, 30, 2785-2791.
- (13) Salomon-Ferrer, R.; Götz, A. W.; Poole, D.; Le Grand, S.; Walker, R. C. Routine microsecond molecular dynamics simulations with AMBER on GPUs. 2. Explicit solvent particle mesh Ewald. J. Chem. Theory Comput. 2013, 9, 3878-3888.
- (14) Case, D. A.; Betz, R. M.; Cerutti, D. S.; Cheatham, T. E., III; Darden, T. A.; Duke, R. E.; Giese, T. J.; Gohlke, H.; Goetz, A. W.; Homeyer, N.; Izadi, S.; Janowski, P.; Kaus, J.; Kovalenko, A.; Lee, T. S.; LeGrand, S.; Li, P.; Lin, C.; Luchko, T.; Luo, R.; Madej, B.; Mermelstein, D.; Merz, K. M.; Monard, G.; Nguyen, H.; Nguyen, H. T.; Omelyan, I.; Onufriev, A.; Roe, D. R.; Roitberg, A.; Sagui, C.; Simmerling, C. L.; Botello-Smith, W. M.; Swails, J.; Walker, R. C.; Wang, J.; Wolf, R. M.; Wu, X.; Xiao, L.; Kollman, P. A. Amber 2016; University of California: San Francisco, CA, 2016.
- (15) Li, P.; Merz, K. M. MCPB.py: A python based metal center parameter builder. J. Chem. Inf. Model. 2016, 56, 599-604.
- (16) Wang, J.; Wolf, R. M.; Caldwell, J. W.; Kollman, P. A.; Case, D. A. Development and testing of a general amber force field. J. Comput. Chem. 2004, 25, 1157-1174.
- (17) Maier, J. A.; Martinez, C.; Kasavajhala, K.; Wickstrom, L.; Hauser, K. E.; Simmerling, C. ff14SB: Improving the accuracy of protein side chain and backbone parameters from ff99SB. J. Chem. Theory Comput. 2015, 11, 3696-3713.
- (18) Roe, D. R.; Cheatham, T. E. PTRAJ and CPPTRAJ: Software for processing and analysis of molecular dynamics trajectory data. J. Chem. Theory Comput. 2013, 9, 3084-3095.
- (19) Similar conformational sampling approaches have been used in previous QM/MM studies, see: (a) Lonsdale, R.; Houghton, K. T.; Żurek, J.; Bathelt, C. M.; Foloppe, N.; de Groot, M. J.; Harvey, J. N.; Mulholland, A. J. Quantum mechanics/molecular mechanics modeling of regioselectivity of drug metabolism in cytochrome P450 2C9. J. Am. Chem. Soc. 2013, 135, 8001-8015. (b) Shaik, S.; Chen, H.; Usharani, D.; Thiel, W. QM/MM studies of structure and reactivity of cytochrome P450 enzymes: Methodology and selected applications. Drug Metabolism Prediction; Wiley, 2014; pp 133-178. (c) Yang, Z.; Yang, S.; Yu, P.; Li, Y.; Doubleday, C.; Park, J.; Patel, A.; Jeon, B. S.; Russell, W. K.; Liu, H. W.; Russell, D. H.; Houk, K. N. Influence of water and enzyme SpnF on the dynamics and energetics of the ambimodal [6+4]/[4+2] cycloaddition. Proc. Natl. Acad. Sci. U.S.A. 2018, 115, No. E848. (d) Garcia-Borràs, M.; Houk, K. N.; Jiménez-Osés, G. Computational design of protein function. Computational Tools for Chemical Biology; Royal Society of Chemistry, 2018; pp 87-107. (e) Wang, X.; Zhang, C.; Jiang, Y.; Wang, W.; Zhou, Y.; Chen, Y.; Zhang, B.; Tan, R. X.; Ge, H. M.; Yang, Z. J.; Liang, Y. Influence of water and enzyme on the post-transition state bifurcation of NgnDcatalyzed ambimodal [6+4]/[4+2] cycloaddition. J. Am. Chem. Soc. 2021, 143, 21003-21009. (f) Garcia-Borràs, M.; Kan, S. B. J.; Lewis, R. D.; Tang, A.; Jimenez-Osés, G.; Arnold, F. H.; Houk, K. N. Origin and control of chemoselectivity in cytochrome c catalyzed carbene transfer into Si-H and N-H bonds. J. Am. Chem. Soc. 2021, 143, 7114-7123.
- (20) Chung, L. W.; Sameera, W. M. C.; Ramozzi, R.; Page, A. J.; Hatanaka, M.; Petrova, G. P.; Harris, T. V.; Li, X.; Ke, Z.; Liu, F.; Li, H.-B.; Ding, L.; Morokuma, K. The ONIOM method and its applications. Chem. Rev. 2015, 115, 5678-5796.
- (21) Frisch, M. J.; Trucks, G. W.; Schlegel, H. B.; Scuseria, G. E.; Robb, M. A.; Cheeseman, J. R.; Scalmani, G.; Barone, V.; Petersson, G. A.; Nakatsuji, H.; Li, X.; Caricato, M.; Marenich, A. V.; Bloino, J.; Janesko, B. G.; Gomperts, R.; Mennucci, B.; Hratchian, H. P.; Ortiz, J. V.; Izmaylov, A. F.; Sonnenberg, J. L.; Williams, D.-Y.; Ding, F.; Lipparini, F.; Egidi, F.; Goings, J.; Peng, B.; Petrone, A.; Henderson, T.; Ranasinghe, D.; Zakrzewski, V. G.; Gao, J.; Rega, N.; Zheng, G.; Liang, W.; Hada, M.; Ehara, M.; Toyota, K.; Fukuda, R.; Hasegawa, J.; Ishida, M.; Nakajima, T.; Honda, Y.; Kitao, O.; Nakai, H.; Vreven, T.; Throssell, K.; Montgomery, J. A., Jr.; Peralta, J. E.; Ogliaro, F.; Bearpark, M. J.; Heyd, J. J.; Brothers, E. N.; Kudin, K. N.; Staroverov,

- V. N.; Keith, T. A.; Kobayashi, R.; Normand, J.; Raghavachari, K.; Rendell, A. P.; Burant, J. C.; Iyengar, S. S.; Tomasi, J.; Cossi, M.; Millam, J. M.; Klene, M.; Adamo, C.; Cammi, R.; Ochterski, J. W.; Martin, R. L.; Morokuma, K.; Farkas, O.; Foresman, J. B.; Fox, D. J. Gaussian 16, Rev. C.01; Gaussian Inc.: Wallingford, CT, 2016.
- (22) Lian, P.; Johnston, R. C.; Parks, J. M.; Smith, J. C. Quantum chemical calculation of pKas of environmentally relevant functional groups: Carboxylic acids, amines, and thiols in aqueous solution. J. Phys. Chem. A 2018, 122, 4366-4374.
- (23) Chen, K.; Zhang, S.-Q.; Brandenberg, O. F.; Hong, X.; Arnold, F. H. Alternate heme ligation steers activity and selectivity in engineered cytochrome P450-catalyzed carbene-transfer reactions. J. Am. Chem. Soc. 2018, 140, 16402-16407.
- (24) (a) Becke, A. D., III Density-functional thermochemistry. III. The role of exact exchange. J. Chem. Phys. 1993, 98, 5648-5652. (b) Lee, C.; Yang, W.; Parr, R. G. Development of the Colle-Salvetti correlation-energy formula into a functional of the electron density. Phys. Rev. B: Condens. Matter Mater. Phys. 1988, 37, 785-789.
- (25) Vreven, T.; Frisch, M. J.; Kudin, K. N.; Schlegel, H. B.; Morokuma, K. Geometry optimization with QM/MM methods II: Explicit quadratic coupling. Mol. Phys. 2006, 104, 701-714.
- (26) Lin, H.; Truhlar, D. G. QM/MM: What have we learned, where are we, and where do we go from here? Theor. Chem. Acc. 2006, 117, 185-199.
- (27) (a) Logunov, I.; Schulten, K. Quantum chemistry: Molecular dynamics study of the dark-adaptation process in bacteriorhodopsin. J. Am. Chem. Soc. 1996, 118, 9727-9735. (b) Rommel, J. B.; Kästner, J. The fragmentation-recombination mechanism of the enzyme glutamate mutase studied by QM/MM simulations. J. Am. Chem. Soc. 2011, 133, 10195-10203. (c) Saura, P.; Suardíaz, R.; Masgrau, L.; Lluch, J. M.; González-Lafont, A. Unraveling how enzymes can use bulky residues to drive site-selective C-H activation: The case of mammalian lipoxygenases catalyzing arachidonic acid oxidation. ACS Catal. 2014, 4, 4351-4363. (d) Cooper, A. M.; Kästner, J. Averaging techniques for reaction barriers in QM/MM simulations. Chem-PhysChem 2014, 15, 3264-3269.
- (28) Lippert, G.; Hutter, J.; Parrinello, M. Michele A hybrid Gaussian and plane wave density functional scheme. Mol. Phys. 1997, 92, 477-487.
- (29) Kühne, T. D.; Iannuzzi, M.; Del Ben, M.; Rybkin, V. V.; Seewald, P.; Stein, F.; Laino, T.; Khaliullin, R. Z.; Schütt, O.; Schiffmann, F.; Golze, D.; Wilhelm, J.; Chulkov, S.; Bani-Hashemian, M. H.; Weber, V.; Borštnik, U.; Taillefumier, M.; Jakobovits, A. S.; Lazzaro, A.; Pabst, H.; Müller, T.; Schade, R.; Guidon, M.; Andermatt, S.; Holmberg, N.; Schenter, G. K.; Hehn, A.; Bussy, A.; Belleflamme, F.; Tabacchi, G.; Glöß, A.; Lass, M.; Bethune, I.; Mundy, C. J.; Plessl, C.; Watkins, M.; VandeVondele, J.; Krack, M.; Hutter, J. CP2K: An electronic structure and molecular dynamics software package - Quickstep: Efficient and accurate electronic structure calculations. J. Chem. Phys. 2020, 152, 194103.
- (30) (a) Himo, F. Recent trends in quantum chemical modeling of enzymatic reactions. J. Am. Chem. Soc. 2017, 139, 6780-6786. (b) Sheng, X.; Himo, F. Enzymatic Pictet-Spengler reaction: Computational study of the mechanism and enantioselectivity of Norcoclaurine Synthase. J. Am. Chem. Soc. 2019, 141, 11230-11238.
- (31) Becke, A. D. Density-functional exchange-energy approximation with correct asymptotic behavior. Phys. Rev. A: At., Mol., Opt. Phys. 1988, 38, 3098-3100.
- (32) Grimme, S.; Antony, J.; Ehrlich, S.; Krieg, H. A consistent and accurate ab initio parametrization of density functional dispersion correction (DFT-D) for the 94 elements H-Pu. J. Chem. Phys. 2010, 132, 154104.
- (33) VandeVondele, J.; Hutter, J. Gaussian basis sets for accurate calculations on molecular systems in gas and condensed phases. J. Chem. Phys. 2007, 127, 114105.
- (34) Goedecker, S.; Teter, M.; Hutter, J. Separable dual-space Gaussian pseudopotentials. Phys. Rev. B: Condens. Matter Mater. Phys. **1996**, *54*, 1703–1710.

- (35) Bussi, G.; Laio, A. Using metadynamics to explore complex free-energy landscapes. Nat. Rev. Phys. 2020, 2, 200-212.
- (36) (a) den Otter, W. K.; Briels, W. J. The calculation of freeenergy differences by constrained molecular-dynamics simulations. J. Chem. Phys. 1998, 109, 4139-4146. (b) Sprik, M.; Ciccotti, G. Free energy from constrained molecular dynamics. J. Chem. Phys. 1998, 109, 7737-7744.
- (37) (a) Shaik, S.; Lai, W.; Chen, H.; Wang, Y. The valence bond way: Reactivity patterns of cytochrome P450 enzymes and synthetic analogs. Acc. Chem. Res. 2010, 43, 1154-1165. (b) Schröder, D.; Shaik, S.; Schwarz, H. Two-state reactivity as a new concept in organometallic chemistry. Acc. Chem. Res. 2000, 33, 139-145.
- (38) (a) Dhuri, S. N.; Cho, K.-B.; Lee, Y.-M.; Shin, S. Y.; Kim, J. H.; Mandal, D.; Shaik, S.; Nam, W. Interplay of experiment and theory in elucidating mechanisms of oxidation reactions by a nonheme Ru^{IV}O complex. J. Am. Chem. Soc. 2015, 137, 8623-8632. (b) Shaik, S.; Hirao, H.; Kumar, D. Reactivity of high-valent iron-oxo species in enzymes and synthetic reagents: A tale of many states. Acc. Chem. Res. 2007, 40, 532-542.
- (39) (a) Ogliaro, F.; Harris, N.; Cohen, S.; Filatov, M.; de Visser, S. P.; Shaik, S. A model "rebound" mechanism of hydroxylation by cytochrome P450: Stepwise and effectively concerted pathways, and their reactivity patterns. J. Am. Chem. Soc. 2000, 122, 8977-8989. (b) de Visser, S. P.; Kumar, D.; Cohen, S.; Shacham, R.; Shaik, S. A predictive pattern of computed barriers for C-H hydroxylation by compound I of cytochrome P450. J. Am. Chem. Soc. 2004, 126, 8362-8363. (c) Hirao, H.; Kumar, D.; Thiel, W.; Shaik, S. Two states and two more in the mechanisms of hydroxylation and epoxidation by cytochrome P450. J. Am. Chem. Soc. 2005, 127, 13007-13018. (d) Shaik, S.; Kumar, D.; de Visser, S. P. A valence bond modeling of trends in hydrogen abstraction barriers and transition states of hydroxylation reactions catalyzed by cytochrome P450 enzymes. J. Am. Chem. Soc. 2008, 130, 10128-10140. (e) Caddell Haatveit, K.; Garcia-Borràs, M.; Houk, K. N. Computational protocol to understand P450 mechanisms and design of efficient and selective biocatalysts. Front. Chem. 2018, 11, 663. (f) Wu, X.; Chen, Y.; Wang, X.; Wei, W.; Liang, Y. Origin of site selectivity in toluene hydroxylation by cytochrome P450 enzymes. J. Org. Chem. 2021, 86, 13768-13773.
- (40) (a) Wheeler, S. E.; Houk, K. N.; Schleyer, P. v. R.; Allen, W. D. A hierarchy of homodesmotic reactions for thermochemistry. J. Am. Chem. Soc. 2009, 131, 2547-2560. (b) Bach, R. D. Ring strain energy in the cyclooctyl system. The effect of strain energy on [3 + 2]cycloaddition reactions with azides. J. Am. Chem. Soc. 2009, 131, 5233-5243. (c) Fu, Y.; Zerull, E. E.; Schomaker, J. M.; Liu, P. Origins of catalyst-controlled selectivity in Ag-catalyzed regiodivergent C-H amination. J. Am. Chem. Soc. 2022, 144, 2735-2746.
- (41) Attempts to locate the interconversion transition state between 4_{pro-R} and 4_{pro-S} using QM/MM were not successful. Scanning of the reaction coordinate using QM/MM suggests that the isomerization has a low barrier of ca. 2.8 kcal/mol with respect to 4_{pro-R}. See Figure \$15 in the Supporting Information.
- (42) Based on DFT calculations on model Fe-porphine systems, the formation of six-membered cyclic 1,3-diamine products (Figure S16) and many previously reported enzymatic $C(sp^3)$ -H amination reactions also have relatively high barriers to C-N bond forming radical rebound ($\Delta G^{\ddagger}_{\text{rebound}} > 8.2 \text{ kcal/mol.}$ See refs 6e–6g and Table S2 for a summary). Therefore, the enantioselectivity-determining steps in these enzymatic C(sp3)-H amination reactions may be affected by the relative rates of C-N radical rebound and conformational change of the radical intermediates.